

STRUCTURAL BIOLOGY

Conformational dynamics of a G protein–coupled receptor helix 8 in lipid membranes

Patricia M. Dijkman^{1*}, Juan C. Muñoz-García^{1†‡}, Steven R. Lavington¹, Patricia Suemy Kumagai^{1,2}, Rosana I. dos Reis^{1§}, Daniel Yin¹, Phillip J. Stansfeld^{3,4}, Antonio José Costa-Filho⁵, Anthony Watts^{1||}

G protein-coupled receptors (GPCRs) are the largest and pharmaceutically most important class of membrane proteins encoded in the human genome, characterized by a seven-transmembrane helix architecture and a C-terminal amphipathic helix 8 (H8). In a minority of GPCR structures solved to date, H8 either is absent or adopts an unusual conformation. The controversial existence of H8 of the class A GPCR neurotensin receptor 1 (NTS1) has been examined here for the nonthermostabilized receptor in a functionally supporting membrane environment using electron paramagnetic resonance, molecular dynamics simulations, and circular dichroism. Lipid-protein interactions with phosphatidylserine and phosphatidylethanolamine lipids, in particular, stabilize the residues 374 to 390 of NTS1 into forming a helix. Furthermore, introduction of a helix-breaking proline residue in H8 elicited an increase in β-arrestin–NTS1 interactions observed in pull-down assays, suggesting that the structure and/or dynamics of H8 might play an important role in GPCR signaling.

Copyright © 2020
The Authors, some
rights reserved;
exclusive licensee
American Association
for the Advancement
of Science. No claim to
original U.S. Government
Works. Distributed
under a Creative
Commons Attribution
NonCommercial
License 4.0 (CC BY-NC).

INTRODUCTION

G protein-coupled receptors (GPCRs) are of considerable biological and pharmacological significance, since they account for ~1% of human genome-encoded proteins and are implicated in a variety of biological processes and pathologies (1). In recent years, GPCR structural biology has undergone rapid progress as a result of advances in protein engineering, the use of lipidic cubic phases and x-ray free-electron lasers for crystallography, and most recently, developments in cryo-electron microscopy (cryo-EM) (2), resulting in structures for 57 unique receptors published to date. In all cases, GPCRs are characterized by a seven-transmembrane helix architecture, with the majority of structures displaying an additional structural element, helix 8 (H8). H8 is an amphipathic α helix that follows the conserved NPxxY motif on transmembrane helix 7 (TM7). Sequence alignment of class A GPCRs reveals a semi-conserved motif F(R/K)xx(F/L)xxx(L/F) for H8 (fig. S1). Physiological studies have shown H8 to be important for surface expression of GPCRs, for receptor trafficking, and for G protein activation and specificity thereof (3–7). Moreover, biophysical studies of the μ opioid receptor (8, 9) and rhodopsin (10–12) suggest that the conformational

dynamics of H8 are involved in GPCR (pre-)activation and interaction with arrestin (12).

Given the potential functional significance of H8, it is noteworthy that in a minority of structures, H8 either is absent or adopts an unusual conformation (fig. S1 and table S1); of the 367 structures of class A GPCRs published to date, all but 30 (~8%), representing 17 (~30%) of the 57 unique class A GPCRs for which structures have been published, show a helical H8. In some cases, this can be rationalized by the lack of sequence determinants, but for several receptors, specifically, the adenosine A1 receptor (A1R), the angiotensin II type 1 and type 2 receptors (AT1R and AT2R, respectively), the CC chemokine receptor type 2, the D₄ dopamine receptor, the purinergic P2Y12 receptor (P2Y12R), and the rat neurotensin receptor 1 (NTS1), one or more of the reported structures lack H8 despite the presence of an intact H8 motif (fig. S1). The rat NTS1 is of particular interest, since eight crystal structures have been published to date, demonstrating distinct conformations of H8 (table S2) (13–16). In all cases, thermostabilizing mutations and C-terminal and/or intracellular loop 3 (IC3) truncations were necessary for crystallization of NTS1, with four of the crystal constructs also containing T4-lysozyme (T4L) insertions (table S2) (13, 15, 16). Crystallographic studies of NTS1 using constructs in which functionally impairing mutations were reverted back to wild-type (WT) (15), or with alternative thermostabilizing mutations lacking a T4L insertion, which showed improved functionality (14), did show the presence of H8.

Here, we sought to determine the conformation adopted by the H8 residues in an NTS1 construct having the full-length C terminus and no thermostabilizing mutations, as well as the influence of the lipid environment and receptor activation state on this conformation. A combination of continuous-wave electron paramagnetic resonance (CW-EPR), circular dichroism (CD), and molecular dynamics (MD) demonstrate that NTS1 has a dynamic H8 that is dependent on lipid-protein interactions for its helicity. Furthermore, agonist binding to the receptor induces (subtle) rearrangements of the helix, and disruption of helical structure by a proline mutation affects NTS1–arrestin binding in human embryonic kidney (HEK) 293T cells. Together, these results emphasize the importance of lipids in H8 structure and the dynamic nature of H8 in NTS1.

¹Biomembrane Structure Unit, Department of Biochemistry, University of Oxford, South Parks Road, Oxford OX1 3QU, UK. ²Instituto de Física de São Carlos, Universidade de São Paulo, Av. Trabalhador São-Carlense 400, C.P. 369, São Carlos SP 13560-970, Brazil. ³Department of Biochemistry, University of Oxford, South Parks Road, Oxford OX1 3QU, UK. ⁴School of Life Sciences & Department of Chemistry, University of Warwick, Coventry CV4 7AL, UK. ⁵Departamento de Física, Faculdade de Filosofia, Ciências e Letras de Ribeirão Preto, Universidade de São Paulo, Av. Bandeirantes 3900, Ribeirão Preto SP 14040-901, Brazil.

*Present address: Max Planck Institute for Biophysics, Max-von-Laue-Straße 3, 60438 Frankfurt am Main, Germany; Institute of Neuropathology, University Medical Center Göttingen, Robert-Koch-Straße 40, 37075 Göttingen, Germany; Cluster of Excellence “Multiscale Bioimaging: from Molecular Machines to Networks of Excitable Cells” (MBEExC), University of Göttingen, Robert-Koch-Straße 40, 37075 Göttingen, Germany.

†These authors contributed equally to this work.

‡Present address: School of Pharmacy, University of East Anglia, Norwich Research Park, Norwich NR4 7TJ, UK.

§Present address: National Physical Laboratory, Hampton Road, Teddington TW11 0LW, UK.

||Corresponding author. Email: anthony.watts@bioch.ox.ac.uk

RESULTS**CW-EPR reveals helical periodicity for H8**

CW-EPR was used to probe the secondary structure and conformational dynamics of H8 in NTS1 reconstituted into a lipid bilayer and lacking any thermostabilizing mutations that were previously required for crystallization (table S2) (13–16). Specifically, cysteine mutations for site-directed spin labeling with 2,2,5,5-tetramethylpyrroline-1-oxyl-3-methyl)methanethiosulfonate (MTSL) (R1) were introduced into a background mutant of NTS1 (Δ C-NTS1) in which native accessible cysteines were mutated to serine or alanine residues (C172S^{3,55}, C278S^{IC3}, C332S^{6,59}, C386S^{C-term}, and C388A^{C-term}). The background mutant shows the same affinity for agonist as WT receptor [dissociation constant (K_d) \leq 2 nM] (17), single-cysteine mutants thereof were previously shown to be able to bind $G\alpha_{i1}$ in a guanosine 5'-O-(3'-thiotriphosphate)-dependent manner (17), and all single-cysteine mutants used here showed salt-sensitive binding to a ligand affinity column, as expected for functional NTS1, although signaling competence was not tested. CW-EPR spectra were recorded at 295 and 170 K (figs. S2 and S3, respectively) for NTS1 sequentially spin-labeled at the C-terminal residues 374 to 393 reconstituted in brain polar lipid (BPL) extract liposomes. NTS1 has previously been shown to be functional within this lipid environment (18).

All spectra were complex, containing multiple dynamic components; a more ($\tau_c \approx$ 30 to 200 ns) and a less ($\tau_c \approx$ 2 ns) motionally restricted component, labeled “i” and “m,” respectively (fig. S2), can be distinguished. These two components could arise from different conformational states of the receptor or from spin label rotamers with different interactions with their environment, resulting in different amplitude of motion, rate of motion, or both (19). Changes in the intensity of these components reflect changes in the population of the corresponding protein states or spin label rotamers. The outer splittings ($2A_{zz'}$) reflect the mobility of the more restricted component “i,” while the width of the central resonance line (ΔH_0) is only somewhat biased by the more mobile spectral component “m,” and is a good overall measure of spin label mobility (fig. S2) (10, 19).

As the mobility of the spin label, and thus ΔH_0 , is dependent on its local environment, the secondary structure of a sequence can be assessed from the periodicity in this mobility parameter (10). Plotting the inverse of the central linewidth against residue number shows that ΔH_0^{-1} , for part of the probed stretch, follows a sine function, indicative of helical periodicity (Fig. 1A). To determine the length of the helix, sine functions were fit to all possible residue stretches between 4 and 20 residues long, and fitting results were ranked according to the residual sum of squares. The periodicity in ΔH_0^{-1} for apo receptor was most consistent with two helical stretches kinked around residues F380-L381 (Fig. 1A). The data in the presence of saturating concentrations of agonist, neurotensin (NT; Fig. 1B), were consistent with an uninterrupted helix, and in both cases, the periodicity was approximately 3.6 residues (Fig. 1, A and B, dotted lines). No clear periodicity could be discerned beyond residue W391, which follows helix-breaking residues P389 and G390, suggesting that the rest of the probed C terminus lacks regular structure. Compared to the apo state, the presence of agonist elicited the largest changes in the local dynamics of the residues flanking the putative helix kink (380 to 382) as gauged by the observed differences in ΔH_0^{-1} and the relative contributions of the more and less motionally restricted spectral components (Fig. 1, B to F, and fig. S2). Addition

of NT resulted in either an increase in local dynamics (increase in ΔH_0^{-1} , residue 381; Fig. 1, C and E) or a decrease (residues 380 and 382; Fig. 1, C, D, and F). The observation of opposite effects on spin label mobility for alternating residues (378 to 383; Fig. 1C) may reflect a local reorientation of the helix relative to the membrane, allowing the formation of an uninterrupted helix. An increase in ΔH_0^{-1} in the presence of NT compared to apo receptor was observed for most label positions on the C-terminal half of H8 (from 383 onward) and the unstructured C-terminal stretch beyond H8, suggesting an overall increase in spin label mobility in the presence of agonist (Fig. 1C), although the effect of agonist on the spectra was modest (fig. S2).

H8 secondary structure is stabilized by membranes

To assess the influence of the membrane on the secondary structure of H8, a peptide corresponding to H8 (S373-C388) was studied by far-ultraviolet (UV) CD in aqueous buffer, in detergent, and in liposomal suspensions of 1-palmitoyl-2-oleoyl-*sn*-glycero-3-phosphocholine (POPC) or the more native BPL. In the absence of detergent or lipid (black line; Fig. 2), the CD spectrum is characteristic of an unstructured peptide ($8 \pm 1\%$ helical; fig. S4A), showing a strong negative signal around 200 nm. However, in the presence of lipids (red and gray lines; Fig. 2) or detergents (fig. S4A), the peptide shows a higher propensity to adopt a helical secondary structure (~29 to 65% helical; fig. S4A). Although it has to be noted that the very low lipid-to-protein ratio (5:1, mol:mol) used to minimize scattering in the far-UV region of the spectrum means that the spectra are likely to be subject to flattening, affecting the reliability of detailed spectral analysis, the differences between the spectra in the presence and absence of lipid are a clear indication of the stabilizing effect of lipid membranes on the secondary structure of this amphipathic helix.

The type of lipid used influenced the CD spectra of the NTS1 H8 peptide. The blue shift of ~2 nm in the zero crossing ($\Delta\varepsilon = 0$) observed in the presence of POPC compared to BPL (Fig. 2) is indicative of reduced α -helical content ($29 \pm 2\%$ and $34 \pm 1\%$ followed from spectral analysis for POPC and BPL, respectively). Furthermore, while the shape of the CD spectrum of the peptide in the presence of POPC was similar to that of the peptide in detergent, the presence of BPL resulted in a more pronounced CD signal at ~225 nm (Fig. 2 and fig. S4A). These results suggest that other types of lipid present in BPL besides phosphatidylcholine (PC) lipids, e.g., phosphatidylethanolamine (PE) or phosphatidylserine (PS) lipids, constituting ~33 and ~19% of BPL, respectively, could have stabilizing interactions with H8.

H8 interacts predominantly with lipid headgroups

To determine the depth of H8 penetration into lipid bilayers, the effect of the S373-C388 H8 peptide on acyl chain order of POPC model membranes was examined using EPR and spin-labeled PC lipids [1-palmitoyl-2-stearoyl-(5/12/14-doxyl)-*sn*-glycero-3-phosphocholine (DOXYL-PC)]. Large unilamellar vesicles (LUVs; 100 nm) were formed, with a DOXYL-PC spin label specifically installed in either the outer or inner leaflet of the vesicle (20). EPR spectra were recorded in the absence and presence of H8 peptide (fig. S4B), and the apparent order parameters S_{app} , derived from the hyperfine splittings of the spectra (21), were calculated (Table 1). The greatest increase of S_{app} , indicating decreased motional freedom, was observed in the peptide-accessible outer leaflet of the model membrane compared to the peptide-inaccessible inner leaflet. The greatest increase (+15%)

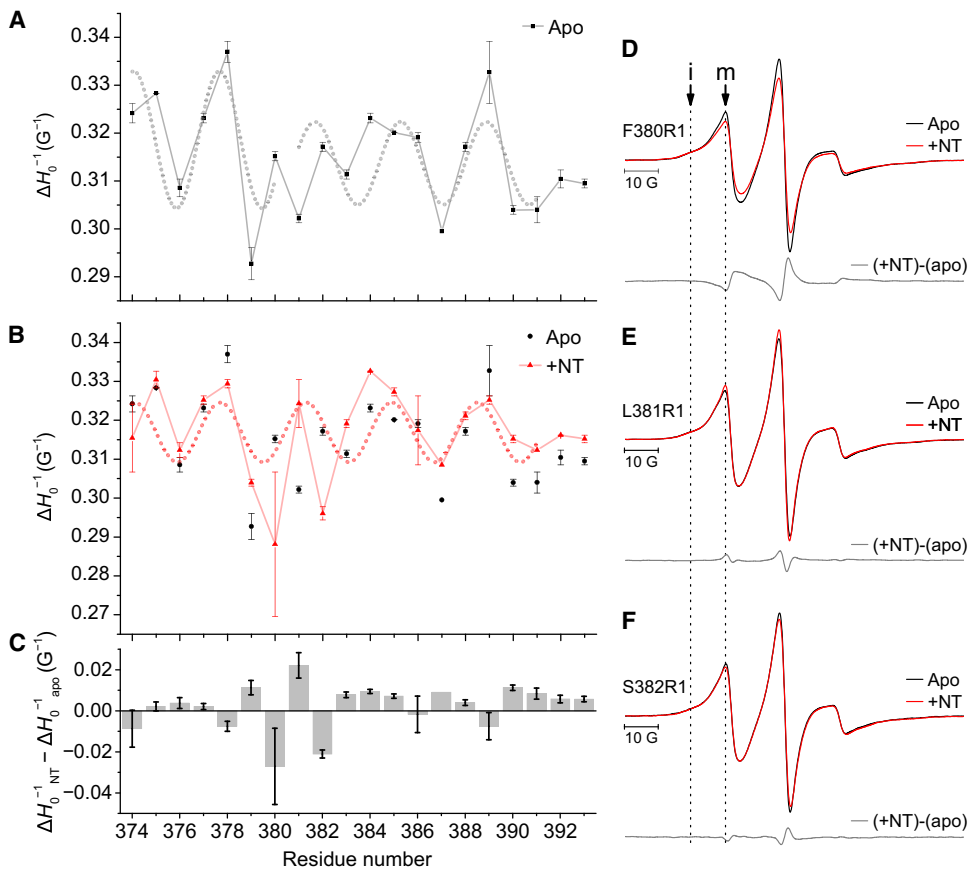


Fig. 1. CW-EPR analysis of H8 periodicity. Sequential single cysteine mutants of NTS1 were labeled with MTSL, generating the R1 side chain. EPR spectra were recorded at 295 K for residues along the C-terminal stretch after TM7, encompassing the putative H8 (see fig. S2). ΔH_0^{-1} determined from spectra of NTS1 (A) in the absence (apo, black squares) or (B) presence (+NT, red triangles) of agonist recorded at 295 K is shown here, plotted against residue number. ΔH_0^{-1} data points for apo receptor (black circles) are also shown in (B) for comparison. The dotted gray and red sinusoids have a period of 3.6 residues. (C) The difference in the mobility parameter ΔH_0^{-1} observed between the spectra recorded in the presence ($\Delta H_0^{-1}_{NT}$) and absence of NT ($\Delta H_0^{-1}_{apo}$) is shown for each residue position. A positive value reflects an increase in local dynamics of the spin label in the presence of agonist with respect to the apo receptor. Error bars represent the SEM ($n = 2$); note that lack of an error bar means that both measurements gave the same value. (D to F) Averaged spectra ($n = 2$) recorded in the absence (black line) and presence of agonist (NT, red lines) and difference spectra [(+NT) - (apo), gray line] are shown for three label positions showing the largest spectral changes in the presence of agonist compared to apo: (D) F380R1, (E) L381R1, and (F) S382R1. The spectra are multicomponent, containing a more and less motionally restricted component, labeled "i" and "m," respectively.

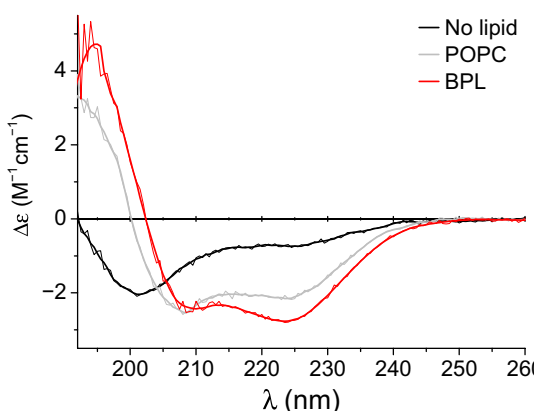


Fig. 2. CD analysis of influence of membrane mimetic on H8 secondary structure. The molar CD ($\Delta\epsilon$) of a peptide (0.1 mg/ml) corresponding to a short NTS1 C-terminal stretch (S373-C388) including the H8 sequence was measured in saline buffer in the absence of lipids (black line) and in the presence of POPC (gray line) or BPL extract (red line) liposomes at a 5:1 lipid-to-peptide molar ratio. Smoothed data (fat line) are plotted on top of the raw data.

was observed with lipids labeled with DOXYL in the 5-position of the carbon chain, closest to the external headgroup region. A more modest increase was observed at the 12- and 14-positions of the outer leaflet (+4.0% and 3.7%, respectively). Barely any ordering was observed at the 5-, 12-, and 14-positions of spin-labeled lipids residing in the inner leaflet (0.9%, 1.2% and 0.5%, respectively).

These data suggest that the S373-C388 H8 peptide interacts with zwitterionic model membranes primarily via surface interactions, with minimal insertion of the peptide into the hydrophobic core of the bilayer, consistent with its predicted amphipathic nature. The asymmetry of the order parameters across the membrane suggests that, in LUVs of this lipid composition, H8 does not insert as a transmembrane peptide. The absence of a substantial ordering of the inner leaflet also suggests that the peptide does not cross the membrane to interact with the inner surface of the vesicle.

MD reveals specific lipid-protein interactions stabilizing H8

The role of lipid-protein interactions in the stability of H8 secondary structure was studied in more detail by atomistic MD (AT-MD)

Table 1. Effect of H8 peptide on spin-labeled lipids. Apparent order parameters S_{app} were calculated for lipids spin labeled at different positions and in different leaflets from hyperfine splitting.

S	S_{app} inner leaflet labeled		% Change	S_{app} outer leaflet labeled		% Change
	With H8	Without H8		With H8	Without H8	
5-PCSL	0.542	0.537	+0.9	0.517	0.594	+15.0
12-PCSL	0.189	0.187	+1.2	0.186	0.179	+4.0
14-PCSL	0.136	0.135	+0.5	0.126	0.121	+3.7

simulations of peptides corresponding to H8, specifically, a short H8 peptide (H8p; residues A374-A385) and a longer peptide (eH8p, A374-H393), as well as of the whole receptor. Simulations were run in both a POPC and a BPL-mimicking membrane bilayer consisting of cholesterol, POPC, 1-palmitoyl-2-oleoyl-*sn*-glycero-3-phosphoethanolamine (POPE), and 1-palmitoyl-2-oleoyl-*sn*-glycero-3-phospho-L-serine (POPS) (see the Materials and Methods) for the H8 peptides and the receptor. Analogous simulations in explicit water in the absence of lipids were also run for the H8 peptides. The secondary structure of H8 was tracked along the 200-ns simulations, and any lipid-protein interactions with H8 were investigated. The length of the AT-MD trajectories is within the same dynamic range of anisotropy averaging of the nitroxide spin label motion in CW-EPR (nanosecond) (21) and therefore suitable for comparison with the EPR experiments.

While both H8 peptides (H8p and eH8p) appeared to be fully unstructured in water, in the presence of a BPL-like membrane, predominantly, α - and π -helical conformations were observed along the trajectories (fig. S5, A and B). The initial α -helical structure of H8p and eH8p was completely lost by the end of the trajectories in the presence of only POPC, suggesting that interaction with POPS, POPE, and/or cholesterol can stabilize H8, in agreement with the higher α -helical content observed by CD in the presence of BPL compared to POPC (Fig. 2 and fig. S4A). For both the shorter H8p and the longer eH8p, the helical structure of the N-terminal half of the peptide (376 to 380) appeared more stable than the C-terminal half (>381), with the latter only showing helical tendency during part of the trajectories. The NTS1 model based on the 4BUO structure (14) with thermostabilizing mutations reverted back to the corresponding WT residues showed an α helix for the A374-L384 fragment throughout the 200-ns simulation when embedded in a BPL-like membrane, while the presence of POPC alone only partially stabilized the helix (A374-L381/S382; fig. S5C). During the AT-MD trajectory of the NTS1 model in a BPL-like membrane, H8 remains parallel to the membrane plane with its hydrophobic (residues F376^{8,50}, F380^{8,54}, and L384^{8,58}) and hydrophilic (residues N375^{8,49}, Q378^{8,52}, and S382^{8,56}) side membrane buried and solvent-exposed or at the solvent-membrane interface, respectively (fig. S5D). Also, the packing of H8 with TM1 and TM7 does not deviate substantially from the crystal structure (fig. S5E) (14). In POPC, H8 adopted a different orientation with respect to the TM helix bundle, kinking away further from TM1, when compared to both the 4BUO crystal structure (14) and the AT-MD simulation in a BPL-like membrane (fig. S5E). The limited stability of NTS1 in POPC compared to BPL is also reflected in the backbone fluctuations observed during the AT-MD simulations, where average backbone root mean square deviations (RMSDs) of $1.9 \pm 0.8 \text{ \AA}$ and $0.9 \pm 0.2 \text{ \AA}$ were found for H8 and $4.2 \pm 0.9 \text{ \AA}$ and

$3.5 \pm 0.3 \text{ \AA}$ for the NTS1 model overall within a POPC and a BPL-like membrane, respectively. Again, these observations suggest that interactions of H8 with POPE, POPS, and/or cholesterol play a role in maintaining its secondary structure.

To provide more insight into the conformational dynamics of H8 in a BPL-like lipid membrane and the effects of ligand binding, additional triplicate simulations of the receptor in the apo and the agonist-bound state were run. As before, an α helix was observed for the apo receptor throughout the 200-ns simulation for the A374-L384 fragment, and the average backbone RMSDs of H8 and NTS1 overall ($0.9 \pm 0.2 \text{ \AA}$ and $3.6 \pm 0.3 \text{ \AA}$, respectively) were also in agreement with the previous simulation ($0.9 \pm 0.2 \text{ \AA}$ and $3.5 \pm 0.3 \text{ \AA}$, respectively). In the NT-bound state, a marked increase in mobility was seen for H8 (residues A374-C386) and TM7-H8 (I364-C386) compared to the apo state receptor. While the backbone RMSD of the TM helices shows only a very modest increase from $2.1 \pm 0.2 \text{ \AA}$ in the apo state to $2.3 \pm 0.2 \text{ \AA}$ in the NT-bound state, the RMSDs of H8 and TM7-H8 increased from $0.9 \pm 0.2 \text{ \AA}$ and $0.9 \pm 0.2 \text{ \AA}$ to $1.8 \pm 0.3 \text{ \AA}$ and $2.3 \pm 0.3 \text{ \AA}$, respectively (fig. S6). In addition, H8 loses part of its helical structure, in particular, at the N-terminal end (residues A374-N375/F376), in the simulations of the agonist-bound receptor (fig. S7A); the number of contacts observed between Y7.53 (Y369) and F8.50 (F376) is strongly reduced compared to the apo state from 28 ± 9 to 2 ± 5 contacts; and the angle between TM7 and H8 changes drastically (Fig. 3A). NT makes extensive contacts with a cascade of mostly aromatic residues and two arginine residues at the extracellular (EC) end of TM6 and TM7. While the EC end of TM6 moves toward the receptor core (from residue W321^{6,48} onward), that of TM7 moves outward (fig. S7B), possibly contributing to the observed increase in RMSD in TM7 and H8 of NT-bound NTS1 compared to the apo receptor (fig. S6). Reorientation of Y7.53 toward N7.49 and D2.50 as observed in various active-state structures of GPCRs has been proposed to be a main part of the activation mechanism (22) and was indeed observed in one of the three simulations of NT-bound NTS1, but not in the other two, where Y369^{7,53} was either found in a hydrophobic pocket made up of L106^{2,43}, V309^{6,36}, and V313^{6,40} or made π - π contacts with F380^{8,54} (Fig. 3B). To probe the importance of Y7.53-F8.50 stacking for the stability of H8, triplicate simulations of a Y7.53A mutant of NTS1 in the apo state in BPL-like membranes were run. The Y7.53A mutation lead to a more modest increase in mobility of H8 and TM7 compared to WT receptor than that elicited by the presence of agonist; the backbone RMSDs of H8 and TM7-H8 only increased to $1.1 \pm 0.3 \text{ \AA}$ and $1.3 \pm 0.2 \text{ \AA}$, respectively, compared to $0.9 \pm 0.2 \text{ \AA}$ and $0.9 \pm 0.2 \text{ \AA}$ for WT apo NTS1 and $1.8 \pm 0.3 \text{ \AA}$ and $2.3 \pm 0.3 \text{ \AA}$ for NT-bound NTS1 (fig. S6). While the number of contacts between Y7.53 and F8.50 during the course of the simulation was reduced (21 ± 7

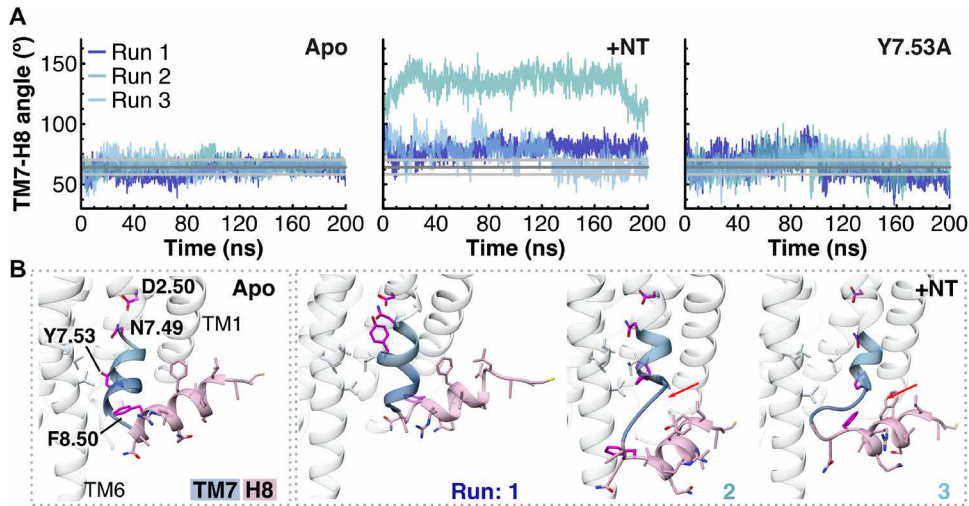


Fig. 3. TM7-H8 angle in MD simulations. (A) The angle between TM7 and H8 calculated between the vector formed by the C α atoms of Y360-N370 (on TM7) and the vector formed by the C α atoms of F376-F380 (on H8) is shown here for all MD simulations. The average angle during the simulations of apo WT NTS1 is shown as a dark gray line in each panel, while the light gray lines indicate the average RMSD of ± 1 SD. (B) The cytosolic end of TM7 (blue) and H8 (pink) are shown for the final frame of one simulation (run 2) of the apo receptor (Apo) and all three simulations of the NT-bound receptor (+NT). While Y7.53 interacts with F8.50 during the simulations of the apo receptor, in the presence of NT, Y7.53 interacts with N7.49 and D2.50 (run 1), or the cytosolic end of TM7 unwinds (runs 2 and 3, red arrow) without Y7.53 interacting with N7.49 and D2.50.

versus 28 ± 9 for WT, a likely reduction with a Bayesian *t* test probability of 0.88), it is still significantly higher than the number of contacts observed for the NT-bound receptor (only 2 ± 5). The angle between TM7 and H8 did increase during the simulations of the Y7.53A mutant and fluctuated more strongly than during the simulations of the WT apo receptor (Fig. 3A). Thus, the Y7.53-F8.50 interaction does appear to have a stabilizing role on H8, but its loss in the agonist-bound state is not the sole cause of the strong effect of agonist on H8 conformational dynamics observed in the AT-MD simulations.

To investigate the role of particular lipid species in the stability of H8, given the observed enhanced stability of H8 in BPL compared to POPC membranes, we looked at the number of close lipid-protein contacts (≤ 3.5 Å) during the simulations, normalizing for the total number of contacts observed and correcting for the relative proportions of each lipid species in the bilayer (Fig. 4). In the apo state, while the whole receptor showed some preference for contacts with POPS over the other phospholipids (fig. S8A), at H8, POPE and, to a lesser extent, POPS were particularly enriched (Fig. 4A and fig. S8B), with most contacts observed at R377^{8,49} and C386^{8,60} (Fig. 4B and fig. S8C); hydrogen bonds and electrostatic interactions were observed between the side chains and the lipid headgroup, phosphate, and/or glycerol moieties (Fig. 4C). These interactions with C386^{8,60} may play a role in preventing the unfolding of the C-terminal end of H8, since in the POPC-only membrane, a shorter H8 was observed. While the Y7.53A mutation did not have a significant effect on the observed lipid-protein contacts compared to the apo WT receptor, in the agonist-bound state, the number of contacts with POPS increased strongly at H8 (Fig. 4A and fig. S8D), but not significantly for the receptor overall (fig. S8, A and D); interactions with the POPS headgroup were seen mainly at R377^{8,49} and C386^{8,60} (Fig. 4C and fig. S8C). The POPS lipid tails also interacted with a number of hydrophobic H8 residues (F380^{8,54}, L381^{8,55}, and L384^{8,58}) and R377^{8,49} (fig. S8C), possibly due to the

change in angle between TM7 and H8 exposing these residues more to the surrounding lipid membrane.

H8 in NTS1 signaling

To gain insight into the role of H8 in NTS1 at the cellular level, WT NTS1, NTS1 with a helix-breaking proline substitution at position V379^{8,53} (NTS1-V379P), and NTS1 with a conservative mutation at the same position (NTS1-V379L) were expressed in HEK293T cells, and the recruitment of β -arrestin-1 was investigated (Fig. 5, A and B). Following NT stimulation, the amount of β -arrestin-1 binding to the receptor was probed using pull-down assays. Our results show a significantly higher amount of β -arrestin-1 bound to the NTS1-V379P compared with the WT NTS1 receptor (Fig. 5A), while no significant difference was found for NTS1-V379L (Fig. 5B). While it appeared that the V379P^{8,53} mutation might also affect extracellular signal-regulated kinases 1 and 2 (ERK1/2) phosphorylation (Fig. 5C), further supporting that H8 could be involved in NTS1-arrestin interactions, the differences in phosphorylation levels between the mutant and WT NTS1 were not statistically significant.

DISCUSSION

Mounting evidence suggests that, in addition to its importance in GPCR biogenesis and trafficking (3–6), H8 may play a role in early GPCR activation (8, 9, 12) and biased signaling through the arrestin pathway (6, 9, 12). Notably, a subset of all class A GPCRs solved to date (30 of 367) did not have a canonical H8 perpendicular to the TM bundle following TM7. Sequence alignment of all crystallized GPCRs shows that for some of these receptors, this may be due to the absence of certain conserved residues of the H8 F^{8,50}(R/K)^{8,51}xx(F/L)^{8,54}xxx(L/F)^{8,58} motif (table S1); the sequences of the leukotriene 4 BLT1 receptor, the lysophosphatidic acid 6 receptor, and free fatty acid 1 receptor (FFA1R) deviate substantially from the canonical sequence, with FFA1R even having a proline residue at

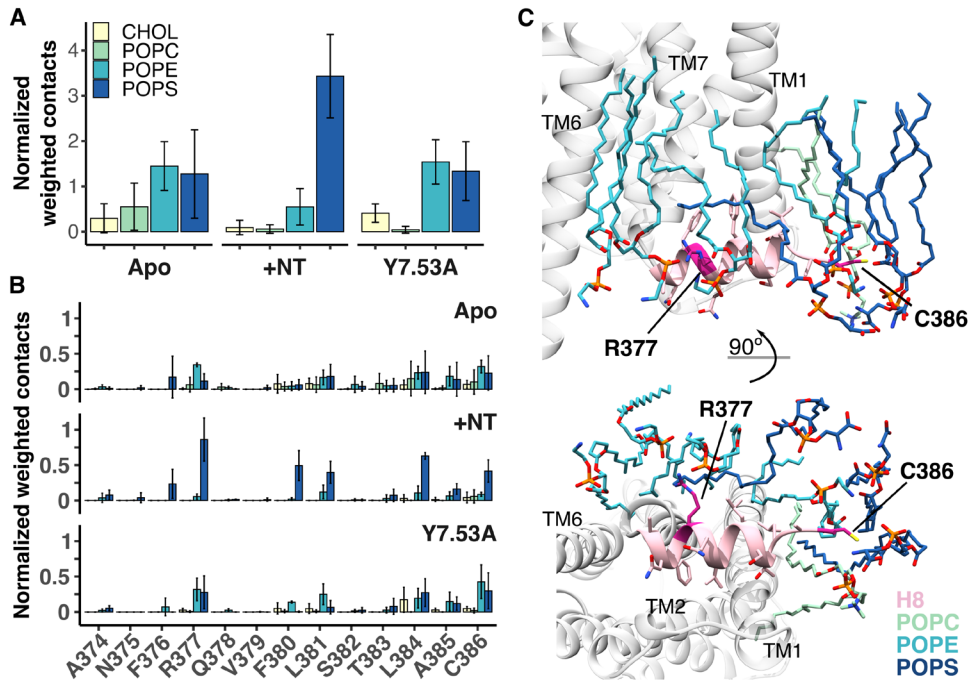


Fig. 4. Lipid-protein interactions observed in MD. (A) The number of lipid-protein contacts ($\leq 3.5 \text{ \AA}$) per lipid species observed during AT-MD simulations of NTS1 in a BPL-like bilayer was normalized by the total number of interactions during each simulation run and weighted by the percentage of each lipid type found in the mixed bilayer. Results are shown for simulations of apo WT NTS1 (Apo), NT-bound WT NTS1 (+NT), and apo mutant NTS1 where Tyr³⁶⁹ is mutated to Ala (Y7.53A). Averages of three simulation runs for each condition for the timeframe in equilibrium (20 to 200 ns) are shown with error bars representing the SD. Contacts are shown (A) for H8 as a whole (residues A374-C386) and (B) for the individual H8 residues. Contacts for the whole receptor, a breakdown of the contacts into contacts with the lipid tails and lipid headgroups, and statistical analysis are shown in fig. S8. (C) Final frame of the AT-MD simulation of apo NTS1 in a BPL-like bilayer, showing NTS1 (gray cartoon) and lipids surrounding H8 (highlighted in pink). POPS (dark blue sticks) and POPE (cyan sticks) lipids are observed clustered around R377^{8,51} (magenta) and the C-terminal C386^{8,60} (magenta) throughout the AT-MD simulations. CHOL, cholesterol.

position 8.50. However, other receptors, such as NTS1, have been crystallized without a structured eighth helix despite showing a (near) canonical H8 sequence. Conversely, receptors with similarly deviating sequences, e.g., the lysophosphatidic acid receptor 1 (MSxxFxxxL), the C5a1 receptor (SLxxNxxxE), or the sphingosine-1-phosphate receptor 1 (MRxxFxxxM), lacking the most conserved Phe, have only been crystallized with a structured H8 (table S1), suggesting that the stability of the helix cannot be rationalized by sequence determinants alone.

Although most of the GPCR structures for which H8 was found to be unstructured were solved using constructs containing an IC3 insertion, and a destabilizing effect of the insertion cannot be excluded, there seems to be no clear correlation between the presence of an IC3 fusion and the absence of H8. Many other GPCRs have been crystallized with a structured H8 despite the presence of an IC3 insertion; not all structures of receptors that have been found to lack a structured H8 were solved using constructs containing an IC3 insertion (e.g., for AT1R, AT2R, and A1R, an N-terminal fusion protein was used instead); and in some cases, the same or similar constructs containing an IC3 insertion have resulted in structures with and without a helical H8 (e.g., for P2Y12R-bRIL and the various thermostabilized forms of NTS1-T4L).

Thus far, 10 receptor subtypes have been crystallized, both with and without a helical H8 (fig. S1). For NTS1, this discrepancy between crystal structures was suggested to reflect the relative low stability of H8 (14) or differences in activation state of the receptor

(15, 23), which were produced using different thermostabilized constructs showing varying degrees of G protein activation (table S2) (13–16). Here, using CW-EPR spectroscopy, we could demonstrate the presence of a helical H8, for a nonthermostabilized, non-C-terminally truncated NTS1 construct reconstituted in lipid bilayers. Helical periodicity was observed stretching from residue A374^{8,48} up to G390^{8,64}/W391^{8,65}, both for the apo receptor and in the presence of agonist. It has to be noted that the Pro-to-Cys mutation and spin labeling required for the EPR measurements at position 389 may have negated any helix-disrupting effect of the native proline, thus extending H8 beyond its native length. However, the observed change in amplitude of ΔH_0^{-1} for the flanking residues G390^{8,64} and W391^{8,65} relative to L387^{8,61} and C388^{8,62}, determined in the presence of the native Pro, follows the trend expected for continuation of the helical periodicity over that stretch of the sequence, suggesting H8 ends shortly after the helix-breaking Pro^{8,63}-Gly^{8,64} residues. In the absence of ligand, the periodicity in the EPR mobility parameters was best fit with a discontinuous helix, with a kink around residues F380^{8,54}/L381^{8,55}. The structured stretch of H8 in NTS1 crystal structures varied from N375^{8,47}-F380^{8,54} at the shortest [Protein Data Bank (PDB) ID 4XES] to A374^{8,48}-L387^{8,61} at the longest (PDB ID 4BV0, chain B; table S2). Notably, the end of the shortest resolved structured H8 coincides with the location of the putative helix kink observed in our EPR experiments.

Previous fluorescence, double electron-electron resonance (DEER), and nuclear magnetic resonance (NMR) spectroscopy studies have

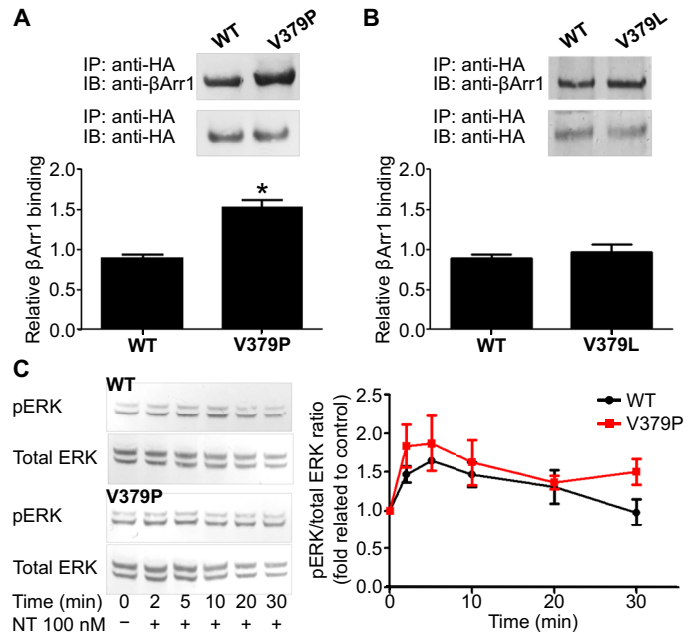


Fig. 5. Association of NTS1 with β-arrestin-1 and extracellular signal-regulated kinases 1 and 2 phosphorylation. (A and B) Pull-down assays were performed to assess the interaction of β-arrestin-1 (βArr1) with the receptor. Specifically, HEK293 cells expressing wild-type NTS1 (WT), NTS1-V379P (V379P), or NTS1-V379L (V379L) receptors were stimulated with 100 nM NT for 15 min at 37°C. After stimulation, cell lysates were precipitated with anti-hemagglutinin (HA) antibody, and Western blotting was performed to probe the amount of β-arrestin-1 interacting with the receptors. Signals were quantified by densitometry, and values were normalized by the amount of β-arrestin-1 interacting with NTS1. Each point represents the mean of four independent experiments, and error bars represent the SEM. Statistical significance was determined using one-way analysis of variance (ANOVA) with Dunnett's multiple comparison test; * $P < 0.05$. IP, immunoprecipitation; IB, immunoblot. (C) Kinetics profiles for extracellular signal-regulated kinases 1 and 2 (ERK1/2) phosphorylation (pERK) after 100 nM NT stimulation in cells expressing WT or V379P are shown. Signals were quantified by densitometry, and pERK values were normalized by total ERK values. Each point represents the mean of three independent experiments, and error bars represent the SEM. Statistical significance was tested using a two-sample two-tailed t test.

suggested that agonist binding alone can trigger changes in the local dynamics of TM7/H8 in a number of different GPCR subtypes (8, 9, 11, 24, 25), independent of the well-described outward movement of TM6 upon GPCR activation (8, 25), suggesting that conformational changes in TM7, H8, and IC1 may precede TM6 movement (8, 25). While the presence of ligand did not affect the overall structure of H8 of NTS1, as gauged here by EPR, it did appear to induce some local dynamic effects. The largest changes were observed for the residues flanking the putative helix kink (F380^{8,54} to S382^{8,56}; Fig. 1 and fig. S2), suggestive of a local rearrangement of H8 possibly resulting in an uninterrupted helix, as implied by the ΔH_0^{-1} periodicity in the presence of agonist. Notably, these changes occur close to the highly conserved F8.50 residue (F376 in NTS1). F8.50 is proposed to interact with the similarly conserved Y7.53 of the NPxxY motif on TM7 in the inactive state of class A GPCRs. It is thought that the interactions between Y7.53 and F8.50 are broken upon activation (22), which may contribute to the changes in H8 dynamics upon activation (8, 9, 11, 24, 25); a slight inward movement of the cytosolic end of TM7 relative to its position in the inactive state has

been observed in crystal structures of the agonist-bound (intermediate) active state of several GPCRs (22), confirming earlier observations by DEER spectroscopy of rhodopsin activation (11). This repositioning of TM7 and concomitant repositioning of the side chain of Y7.53 toward the transmembrane core precluding its interaction with F8.50 has been suggested to lead to steric stabilization of TM6 in its active pose (22). For example, in the various “active-like” agonist-bound rat NTS1 crystal structures, Y7.53 packs against TM2, TM3, and TM6 and does not interact with F8.50 (13, 15). Notably, different conformations of the NPxxY motif were also reported in a recent cryo-EM study of a human NTS1 (hNTS1) construct in two G_i -coupled states of the receptor (26): a canonical and a noncanonical state. While the G protein exhibited a very different binding pose in the noncanonical state, being rotated by about 45° compared to the canonical state, the overall structure of hNTS1 was very similar in both states, with the exception of TM7. In the canonical hNTS1 state, Y7.53 was found in the transmembrane core packing against TM6, as observed in the active-like rat NTS1 structures (13, 15), distorting the NPxxY region of TM7, while in the noncanonical hNTS1 state, Y7.53 adopts a more “inactive-like” conformation similar to the 4BUO NTS1 structure, packing against L105^{2,43} (L106 in rat NTS1 numbering), suggesting that it represents an activation intermediate. Notably, H8 is structured in both hNTS1- G_i structures but shorter in the more active-like canonical state (N8.49-F8.54 versus S8.47-C8.60 in the noncanonical state). In our AT-MD simulations of NT-bound NTS1, the number of contacts between Y7.53 and F8.50 was reduced significantly, and TM7 and H8 were more flexible compared to the apo receptor. Eliminating the π-π stacking interaction by mutation of Y7.53 to Ala had a more modest effect on the flexibility of H8 (fig. S6) and the angle between TM7 and H8 (Fig. 3); indeed, Y7.53A still showed CH-π interactions with F8.50. Thus, it is possible that a change in the interaction between Y7.53 and F8.50 upon ligand binding contributes to a locally more dynamic H8 without affecting its secondary structure, in combination with other destabilizing effects of ligand binding on TM7 (fig. S7). The EPR spectra showed a modest increase in ΔH_0^{-1} in the presence of NT compared to apo receptor for most label positions on the C-terminal half of H8 (from 383 onward) and the unstructured C-terminal stretch beyond H8 (Fig. 1C). Residues 372 to 401 of the C terminus of NTS1 have been shown to be involved in coupling to G_s - and G_i -mediated pathways (27), and deletion of residues 374 to 389 was deleterious to G protein activation in an NTS1- $G_{i/q}$ fusion protein (28). Changes in the local dynamics of H8 may be required for receptor signaling, e.g., facilitating engagement with G protein and/or arrestin. TM7/H8 conformation and/or dynamics were previously shown to be particularly sensitive to arrestin-biased ligands for, e.g., the vasopressin receptor 2 and the μ opioid receptor (8, 24). The finger loop of arrestin was also shown to interact predominantly with the N-terminal part of H8 of opsin (the retinal-free active conformation of rhodopsin) (22). Disruption of H8 by insertion of a helix-breaking proline at position V379 resulted in increased binding of β-arrestin-1 relative to WT receptor (Fig. 5), suggesting that structural integrity or dynamics of H8 may also play a role in NTS1-arrestin interactions. High local mobility of H8 has previously been shown to be required for initial (low-affinity) binding of β-arrestin-1 to rhodopsin (12), while deletion or severe disruption of H8 by replacing the central K^{8,53} with a helix-breaking proline was reported to perturb the interaction of the bradykinin B2 receptor with GPCR kinase 2/3 (GRK 2/3) and β-arrestin-2 (6). Thus, while the presence of H8 appears to be required, structural

changes that increase its local dynamics might facilitate arrestin interaction directly, or indirectly, for example, by making the receptor C terminus more readily accessible for GRKs, although such a hypothesis would require further testing. While no interaction was observed between the α 5 helix of the α subunit of G_s and TM7 or H8 of β_2 -adrenergic receptor (β 2AR), more recent structures of GPCR–G protein complexes [reviewed in (29)] of the A_{2A} adenosine receptor (with mini G_s), μ opioid receptor (with G_i), 5-hydroxytryptamine 1B (5-HT_{1B}) receptor (with G_o), rhodopsin (with G_i), and hNTS1 (with G_{i/q}) (26) do show direct contacts of the G protein with the N-terminal part of H8 similar to that observed for arrestin, suggesting that changes in H8 conformation, positioning, and/or dynamics may play a (receptor-dependent) role in G protein recognition and in arrestin coupling.

It is worth noting that EPR spectra of the N-terminal half of H8 in rhodopsin recorded in a previous study in *n*-dodecyl β -D-maltopyranoside (DDM) micelles (10) show stronger immobilization of the spin labels and larger maximal differences in ΔH_0^{-1} (0.1 to 0.27 versus 0.05) between residue positions compared to NTS1 here, suggesting that H8 may be more dynamic in NTS1 than in rhodopsin. The changes observed in the EPR spectra of rhodopsin H8 upon light activation were substantially more pronounced than those observed for here NTS1. This may reflect the previously proposed difference in energy landscape for activation for rhodopsin and other GPCRs (30); covalent coupling to its inverse agonist precludes basal activity in rhodopsin, resulting in a larger change upon activation. It should also be noted that an absence of large changes in CW-EPR does not preclude conformational changes (e.g., rigid body movements) occurring in NTS1 upon ligand binding. For example, CW-EPR spectra of TM6 of the β 2AR show only small spectral changes upon addition of ligand, or even a G protein mimetic, which were of similar magnitude as those observed here for H8 in apo and NT-bound NTS1 (30), even though crystallography and pulsed EPR measurements have shown large conformational changes under these conditions (22, 29, 30).

Both *in vitro* experiments and simulations suggested that lipid-protein interactions are important for H8 secondary structure integrity; in the absence of lipids, CD and MD showed that a peptide corresponding to H8 was unstructured, while the presence of lipids or detergent supported its helical structure. Similar results have previously been obtained for peptides corresponding to the H8 fragment of the CB1 cannabinoid (31) and the β_2 -adrenergic receptors (32) by CD and NMR spectroscopy, where helicities of ~65 and 31%, respectively, were found in membrane-mimicking environments, similar to the values obtained here by CD (fig. S4A), while the peptides appeared unstructured in water. Furthermore, the H8 peptide showed higher helical propensity by CD in the presence of BPL than in the presence of only PC lipids (Fig. 2), indicating that specific lipid headgroup interactions could contribute to its structure. During MD simulations of NTS1 in a BPL bilayer, close interactions were observed between H8 and all main components of the BPL bilayer (POPC, POPE, POPS, and cholesterol) (Fig. 4 and fig. S8). In vivo, PE and PS lipids are largely confined to the inner leaflet of the plasma membrane (20), and interaction with these lipids in particular appears to contribute to the higher stability of H8 in BPL membranes relative to POPC membranes; frequent interactions with R377^{8,51} and C386^{8,60} were observed both with POPE and POPS during simulations of the apo and the NT-bound receptor, respectively. The presence of a basic residue at position 8.51 is highly conserved in class

A GPCRs (fig. S1), suggesting that this stabilizing lipid-protein interaction may be of general significance. PE lipids have previously been shown to be important for NT binding *in vitro* (18), which may be due to stabilization of the native structure of the receptor. The observed increase in contacts between H8 and PS lipids in the NT-bound state suggests that the agonist-bound conformation is particularly stabilized by interaction with anionic lipids, which have been implicated in promoting NTS1 G protein activity *in vitro* (33). In previous simulations using the structure of the thermostabilized NTS1-GW5 construct that was crystallized without a structured H8 (13) and a WT homology model derived therefrom in POPC bilayers (23), a modeled H8 was reported to be unstable. While this discrepancy with our results most likely reflects the difference in starting model, the lack of stabilizing interactions with other lipid species may also have contributed to the lower H8 stability observed (23).

NTS1 produced in *Escherichia coli* as used here, and as used to produce the 4BUO crystal structure (14), is not posttranslationally modified and thus lacks palmitoylation of the C-terminal cysteine residues. An MD study of the dopamine D2 receptor embedded in lipid raft-like membranes showed that C-terminal palmitoylation enhanced membrane penetration by the H8 backbone, while depalmitoylation enabled H8 to move out into the aqueous environment (34). Our MD simulations suggest that lipid-protein interactions, such as the extensive interactions observed between PE and PS lipids and C386 of NTS1, may stabilize H8 in the absence of palmitoylation at this C-terminal cysteine residue (Fig. 4) and maintain partial insertion of its C-terminal end into the membrane throughout the MD simulation (fig. S5D). Furthermore, the palmitoylation thioester bond is labile, making it a transient posttranslational modification. Previous studies of several GPCRs have established that levels of receptor palmitoylation can be modulated by, e.g., agonist binding [reviewed in (35)], suggesting that this modification is dynamic and regulated and that pools of depalmitoylated receptors exist. In hNTS1, inhibition of palmitoylation has been linked to reduced interaction with G_q and lower levels of ERK1/2 phosphorylation, which was ascribed to diminished localization to structured membrane micro-domains (36). Thus, while palmitoylation of the C-terminal cysteines does not appear to be an essential requirement for H8 helicity, it might have a stabilizing and regulating effect.

In conclusion, this study confirms the presence of a structured H8 in NTS1, both for apo and agonist-bound receptor, which is stabilized by lipid-protein interactions. Whether the fact that H8 was only observed in part of the solved crystal structures is due to protein engineering, crystallographic conditions, lack of specific lipid-protein stabilizing contacts, or inherent flexibility of H8 remains unclear. Accumulating evidence suggests that H8 structure, dynamics, and conformation may play a role in GPCR signaling and, in particular, in arrestin-biased pathways, and the techniques used here could be extended to studies in the presence of signaling partners, such as G proteins or β -arrestins, to shed more light on the structural basis of the activation mechanisms of different GPCR signaling pathways and the role that lipids play therein.

MATERIALS AND METHODS

NTS1 purification, spin labeling, and reconstitution

The rat NTS1 was produced as a fusion construct, NTS1BH₆ (MBP-TEV-rT43NTS1-His₆-TEV-TrxA-His₁₀), where NTS1 is truncated at the N terminus (1 to 42), has a His₆ tag added to its C terminus

and is flanked by tobacco etch virus (TEV) protease recognition sites separating it from its N- and C-terminal fusion partners, maltose-binding protein, and thioredoxin, followed by an additional C-terminal His₁₀ tag, respectively (17). Sequential single-cysteine mutations (for residues 374 to 393) were introduced in a cysteine-depleted background mutant of NTS1BH₆ (C172S^{3,55}, C278S^{IC3}, C332S^{6,59}, C386S^{C-term}, and C388A^{C-term}, where superscripts refer to the Ballosteros-Weinstein numbering), previously described in (17). Cysteine mutants of NTS1BH₆ were expressed in *E. coli* BL21(DE3), purified, and reconstituted as previously described (17). Briefly, NTS1BH₆ was solubilized from *E. coli* cell pellet in 50 mM tris-HCl (pH 7.4), 200 mM NaCl, 30% glycerol (v/v), 1% DDM (w/v), 0.5% CHAPS (w/v), and 0.1% (w/v) cholestryl hemisuccinate (CHS), supplemented with protease inhibitors [leupeptin (2 µg/ml), pepstatin A (2 µg/ml), and aprotinin (3 µg/ml)]. NTS1BH₆ was purified from clarified lysate by immobilized metal affinity chromatography [eluting in 50 mM tris-HCl (pH 7.4), 200 mM NaCl, 10% glycerol (v/v), 0.5% CHAPS (w/v), 0.1% DDM (w/v), 0.1% CHS (w/v), and 500 mM imidazole], after which fusion partners were removed by proteolytic cleavage with TEV protease. The receptor was diluted with salt-free buffer to reduce the NaCl (<70 mM) concentration and further purified by ligand-affinity chromatography using N-terminally Cys-derived NT (Alta Bioscience) immobilized on UltraLink Iodoacetyl Resin (Pierce, Thermo Fisher Scientific), ensuring that the final sample contained only properly folded receptor, capable of ligand binding. The sample was incubated with the resin for at least 2 to 3 hours at 4°C, and impurities were removed by washes with 70 and 150 mM NaCl [50 mM tris-HCl (pH 7.4), 10% glycerol (v/v), 0.1% DDM (w/v), and 0.01% CHS (w/v)], after which NTS1 was eluted with 1 M NaCl. The NT column eluate was incubated with 10 mM dithiothreitol (DTT) for 2 to 3 hours at 4°C and concentrated by loading it on a 1-ml HisTrap Ni²⁺ column, extensively washing (~50 to 90 column volumes) to remove DTT and eluting with 400 mM imidazole. Eluted receptor was then incubated with a 20-fold molar excess of MTSI (Toronto Research Chemicals) spin label over receptor for 45 min at room temperature, after which the sample was buffer-exchanged, and excess label was removed by gel filtration using two 5-ml HiTrap Desalting columns (GE Healthcare) connected in series and equilibrated with 50 mM tris-HCl (pH 7.4), 50 mM NaCl, 10% glycerol (v/v), 0.1% DDM (w/v), 0.01% CHS (w/v), and 1 mM EDTA. The labeled receptor was then reconstituted into 100-nm extruded porcine BPL (Avanti Polar Lipids) liposomes at an initial lipid-to-protein molar ratio of 1750:1 using Bio-Beads SM-2 Resin (Bio-Rad) for detergent removal. Proteoliposomes (containing ~1.5 to 3 nmol of NTS1) were resuspended in 10 µl of liposome buffer [50 mM tris-HCl, 50 mM NaCl, 10% glycerol (v/v), and 1 mM EDTA (pH 7.4)], with or without a 5- to 10-fold molar excess of agonist, NT_{8–13} (Sigma-Aldrich), the active C-terminal fragment of NT. Two biological replicates were prepared for each label position.

CW-EPR on NTS1

Samples were loaded into ~0.5-mm glass capillaries (Sigma-Aldrich), which were flame-sealed at one end before loading. Spectra were recorded on an X-band CW spectrometer (EMX, Bruker). The temperature was controlled (295 or 170 K) using a nitrogen cryostat coupled to a variable temperature unit (Oxford Instruments). Spectra were typically collected with a sweep width of 200 G, at 45 s per scan, and the time constant was adjusted to ~10% of the conversion

time. The modulation amplitude was set to 1 or 3 G for spectra recorded at 295 or 170 K, respectively. Receiver gain was set at 40 to 60 dB, and microwave power was adjusted to avoid saturation (10 mW at 295 K and 0.1 mW at 170 K). Between 10 and 20 scans (recording time ~8 to 15 min) were collected and averaged. Single spectra that were recorded as a control before and after the recording of an averaged spectrum, to verify the stability of the receptor over the course of the measurements, were indistinguishable. Spectra were normalized to the integrated intensity of the absorption spectra. Rotational correlation times (τ_c) were estimated from the maximum outer splitting $2A_{zz}'$ of the spectra recorded at 295 K (see fig. S2) using the method of Freed (21), where the maximum outer splitting of the spectra recorded at 170 K was used to determine the rigid limit $2A_{zz}^R$. To determine ΔH_0 , spectra were smoothed using cubic splines in R (using RStudio) and interpolated, and the global maxima and minima were extracted. Nelder-Mead optimization in R was subsequently used to fit sine functions to $(\Delta H_0)^{-1}$ (average of the two biological repeats) plotted against residue number (374 to 393) for all possible residue stretches, discarding results for stretches shorter than four residues. Results were ranked according to the resulting residual sum of squares.

CW-EPR with spin-labeled lipids

POPC and 5/12/14-PCSL or DOXYL-PC were purchased from Avanti Polar Lipids (Alabaster, AL, USA). Lipids were dissolved in chloroform to give stocks (25 mg/ml) and stored at -20°C. A peptide corresponding to S373-C388 of NTS1 (H8 peptide: Ac-SANFRQVFLSTLACLC-NH₂) was purchased from Peptide Synthetics and used without further purification. LUVs were formed with a spin label installed in the outer leaflet of the membrane; for the inner leaflet, the lipid compositions of the donor and acceptor vesicles are reversed. Specifically, adapting a protocol from Cheng *et al.* (20), donor multilamellar vesicles (MLVs) were prepared by mixing POPC (12 mg, 16 µmol) and DOXYL-PC (0.24 mg, 0.3 µmol) in CHCl₃ and dried under nitrogen and then in vacuo for 1 hour. The dried lipid film was suspended in H₂O (500 µl) to a concentration of 32 µM and left to stand at 40°C for 1 hour, with occasional, gentle vortexing. The MLVs were then incubated with 500 µl of methyl-β-cyclodextrin (MβCD; Sigma-Aldrich, 64 µmol) for 2 hours at 1000 rpm and 50°C using a heated vortexer (Eppendorf Thermomixer Comfort). At the same time, acceptor LUVs were formed by first preparing MLVs of POPC (3 mg, 4 µmol) in H₂O with 20% (w/v) sucrose (500 µl) and then subjected to five freeze-thaw cycles between liquid N₂ and 40°C. The freeze-thawed MLVs were extruded 11 times through 100-nm polycarbonate filters (Avanti Polar Lipids). The sucrose-entrapped vesicles were diluted with H₂O (9 ml) and centrifuged for 2 hours at 190,000g and 40°C, using a Beckman Optima XL-100 K Ultracentrifuge and SW 41 Ti rotor. The pelleted vesicles were then resuspended in H₂O (500 µl) to a final concentration of 8 µM. The sucrose-entrapped LUVs were added to the solution of MβCD-solubilized MLVs, and the resulting suspension was mixed for 30 min at 1000 rpm and 50°C using a heated vortexer. This mixed suspension was then diluted in 9 ml of 4.5% (w/v) sucrose solution and centrifuged for 2 hours at 190,000g and 10°C. The unpelleted MLVs and MβCD were removed in the supernatant, and the exchange LUVs were resuspended in 50 mM phosphate buffer (pH 7.2; 100 µl). H8 peptide in dimethyl sulfoxide (DMSO) was added to give a peptide-to-lipid (P:L) molar ratio of 1:25. The relative concentrations of inner leaflet- and outer leaflet-labeled vesicles were

calculated using fluorescence of 0.1% Rhodamine PE in the acceptor vesicles to ensure that the P:L ratio was the same. An identical volume of DMSO was added to lipid-only samples. The mixed suspension was then diluted in 9 ml of 4.5% (w/v) sucrose solution and centrifuged for 2 hours at 190,000g and 10°C. CW-EPR measurements were carried out at 293 K on an X-band CW spectrometer (EMX, Bruker) fitted with a nitrogen cryostat. The hyperfine splittings A_{par} and A_{per} were obtained from the EPR spectra, and the apparent order parameter S_{app} was calculated according to the equation

$$S_{\text{app}} = \frac{A_{\text{par}} + A_{\text{per}^*} * a'_0}{A_{\text{zz}} - \frac{A_{\text{xx}} - A_{\text{yy}}}{2} a'_0}$$

where A_{zz} , A_{yy} , and A_{xx} are the principal hyperfine splittings (32.9, 5.4, and 5.9 for DOXYL, respectively) of the molecular axes of the spin label

$$\frac{a'_0}{a_0} = \frac{A_{\text{zz}} + A_{\text{xx}} + A_{\text{yy}}}{A_{\text{par}} + A_{\text{per}^*}}$$

is a normalization term for the polarity of the environment, and

$$A_{\text{per}^*} = A_{\text{per}} + \left(1.4 * \left[\frac{1 - (A_{\text{par}} - A_{\text{per}})}{A_{\text{zz}} - \frac{A_{\text{xx}} + A_{\text{yy}}}{2}} \right] \right)$$

accounts for dependence of the hyperfine splittings (A_{per}) on the local polarity (21).

Circular dichroism

For CD measurements, the H8 peptide was dissolved at 15 mg/ml in trifluoroethanol (TFE) and then diluted to 0.1 mg/ml in (i) 20 mM sodium phosphate, 20 mM NaCl buffer, or buffer containing either (ii) POPC liposomes (0.43 mg/ml), (iii) BPL liposomes (0.37 mg/ml) to a 5:1 lipid-to-peptide molar ratio, (iv) 1% octyl β-D glucoside, 0.01% CHS, or (v) 0.1% DDM, 0.01% CHS (w/v). Peptide concentration was measured using absorption at 205 nm. Liposomes were prepared by extrusion through 100-nm polycarbonate filters (Whatman). CD spectra were recorded at 293 K between 190 and 260 nm on a Jasco J-815 Spectropolarimeter using a 1-mm quartz cuvette, a scan rate of 20 nm/min, and a data integration time of 1 s. The recorded spectra were corrected for buffer contribution, accounting for TFE (0.67%) and the appropriate lipid/detergent. The data were smoothed in OriginPro 8.5 (OriginLab) using Savitzky-Golay filtering (10-nm window, second-order polynomial), and the DichroWeb server was used to estimate secondary structure; results from multiple algorithms (K2D, CONTIN, CDSSTR, and SELCON3) and reference datasets (sets 4, 7, SP175, and SMP180) that gave a normalized RMSD below 0.1 were averaged.

MD simulations

The NTS1 crystal structure of highest resolution containing a resolved H8 (PDB code 4BUO) (14) was used as initial conformation (upon ligand removal), and the non-resolved ICI was modeled with the software MODELLER [the model with the best Discrete Optimized Protein Energy (DOPE) score was chosen]. For the simulations of the H8 peptides and NTS1 comparing POPC and BPL, simulations were run using GROMACS (v. 4.6.3). Self-assembly coarse-grained (CG)-MD simulations (37) in a POPC membrane were first performed for

100 ns at 323 K using the MARTINI force field, giving a membrane-embedded protein with about 300 POPC lipids, solvated with water particles and ~150 mM NaCl. The final systems were then converted to atomistic detail using the CG2AT protocol, then bilayer/solvent-equilibrated (with positional restraints on the protein) for 1 ns, and lastly run for a further 200 ns (at 310 K) of AT-MD with the GROMOS96 53a6 force field. The self-assembled POPC CG systems were lipid-exchanged (38) to build the BPL-like membrane models, composed of POPC:POPS:POPE:cholesterol at a ratio of 15:22:39:24, therefore mimicking the composition of BPL extract. The resulting heterogeneous membrane systems were submitted, before conversion back to atomistic, to a 100-ns CG-MD simulation at 323 K using the same parameters as for the POPC CG-MD. Each atomistic system was considered to be in equilibrium after the first 20 ns of AT-MD, based on NTS1 backbone RMSD. Therefore, the trajectory analysis was performed from 20 to 200 ns for each AT-MD simulation, using the GROMACS and VMD tools. Further triplicate simulations were run using apo WT NTS1, NT-bound WT NTS1, and apo mutant NTS1 where Tyr³⁶⁹ is mutated to Ala (Y7.53A), in a BPL-like bilayer as described above with a few differences. Specifically, simulations were run using GROMACS (v.2019), the CHARMM36 force field was used for the AT-MD simulations, and Insane (39) was used to build the BPL-like membrane models (same lipid ratio as in the other simulations); the resulting heterogeneous membrane systems were submitted to a 500-ns CG-MD simulation at 310 K, before conversion back to atomistic. Atomistic simulations of 200 ns were performed in triplicate. Lipid-protein contacts (≤ 3.5 Å) per lipid species observed during MD simulations were quantified for each condition for the timeframe in equilibrium (20 to 200 ns). The number of contacts was normalized by the total number of interactions during each simulation run and subsequently weighted by the percentage of each lipid type found in the mixed bilayer. Averages from the triplicate runs were calculated and subjected to statistical analysis using R (in RStudio) using a Bayesian alternative to the two-sample *t* test, BEST (40).

Pull-down assays

Rat NTS1 receptor was cloned into the pOPINHA vector (a gift from R. Owens, OPPF-UK) using the InFusion cloning method (Clontech). The vector containing the receptor was used as the template to generate V379P and V379L mutants using QuikChange (Stratagene) according to the manufacturer's instructions. The sequence of each construct was confirmed by DNA sequencing.

HEK293T cells were cultivated in Dulbecco's modified Eagle's medium (DMEM; Sigma-Aldrich) supplemented with 10% (v/v) fetal bovine serum and glutamine (2 mM) in a 5% CO₂ environment at 37°C. NTS1, NTS1-V379P, and NTS1-V379L plasmids were transiently transfected into HEK293T cells using Lipofectamine 2000 (Invitrogen) following the manufacturer's instructions. Thirty-six hours after the transfection, cells were serum-starved overnight. Subsequently, cells were stimulated with 100 nM NT (Sigma-Aldrich) during 15 min. Following stimulation, cells were placed on ice, washed with phosphate-buffered saline buffer and lysed with 1 ml of cold buffer [50 mM tris-HCl (pH 7.5), 150 mM NaCl, 1% Nonidet P-40, aprotinin (100 µg/ml), leupeptin (10 µg/ml), 1 mM sodium ortovanadate, and 10 mM sodium fluoride]. After lysis by douncing (20 strokes), the lysates were centrifuged at 4°C, 10,000g for 15 min. The supernatants were incubated with 2 µg of anti-hemagglutinin (HA) antibody (Sigma-Aldrich) for 1 hour at 4°C with agitation. After this period of incubation, 20 µl of precleared protein A/G agarose beads

(Santa Cruz Biotechnology) was added, and samples were rotated for 1 hour at 4°C. Subsequently, beads were centrifuged and washed three times with lysis buffer, and bound proteins were eluted by heating to 85°C with 40 µl of 2X SDS-polyacrylamide gel electrophoresis (SDS-PAGE) sample buffer. A/G agarose beads were pelleted, the eluted supernatants were separated by SDS-PAGE and transferred to nitrocellulose membranes, and Western blotting was performed against β-arrestin-1 (1:1000, BD Biosciences) and the receptor (anti-HA, 1:1000, Sigma-Aldrich). Densitometric values were obtained using ImageJ (<https://imagej.nih.gov/ij/>), and corresponding results were plotted using GraphPad (GraphPad Software Inc.). Statistical significance was determined using one-way analysis of variance (ANOVA) with Dunnett's multiple comparison test using GraphPad Prism. A *P* value of <0.05 was considered statistically significant.

ERK1/2 phosphorylation assays

HEK293T cells were cultivated in DMEM (Sigma-Aldrich) with 10% (v/v) fetal bovine serum and glutamine (2 mM) in a 5% CO₂ environment at 37°C. NTS1 and NTS1-V379P plasmids were transiently transfected into cells using Lipofectamine 2000 (Invitrogen) following the manufacturer's instructions. Twenty-four hours after transfection, 3.0 × 10⁵ transfected cells were seeded on six-well plates in DMEM supplemented with 10% (v/v) serum fetal bovine and glutamine (2 mM) and maintained in a 5% CO₂ environment at 37°C during 12 hours. Subsequently, cells were serum-starved overnight and then stimulated with 100 nM NT for the indicated period of time (0 to 30 min) and analyzed for ERK phosphorylation. After NT stimulation, cells were lysed with lysis buffer consisting of 50 mM tris-HCl (pH 7.4), 150 mM NaCl, 1% Nonidet P-40, and protease inhibitors [leupeptin (10 µg/ml), aprotinin (100 µg/ml), 1 mM sodium orthovanadate, and 10 mM sodium fluoride]. Following homogenization at 4°C during 30 min, cellular lysate was centrifuged at 4°C, 13,000g for 15 min, and total protein was quantified by bicinchoninic acid (BCA) assay (Thermo Fisher Scientific). After that, 30 µg of total protein was separated by SDS-PAGE and transferred to nitrocellulose membrane, and Western blotting was performed against total ERK and phosphorylated ERK (pERK, both antibodies from Cell Signaling Technology). Densitometric values obtained with ImageJ (<https://imagej.nih.gov/ij/>) were used to calculate the ratio of pERK to total ERK, and corresponding results were plotted using GraphPad (GraphPad Software Inc.). Statistical significance was tested using a two-sample two-tailed *t* test using GraphPad Prism.

SUPPLEMENTARY MATERIALS

Supplementary material for this article is available at <http://advances.sciencemag.org/cgi/content/full/6/33/eaav8207/DC1>

[View/request a protocol for this paper from Bio-protocol.](#)

REFERENCES AND NOTES

1. A. S. Hauser, M. M. Attwood, M. Rask-Andersen, H. B. Schiöth, D. E. Gloriam, Trends in GPCR drug discovery: New agents, targets and indications. *Nat. Rev. Drug Discov.* **16**, 829–842 (2017).
2. D. M. Thal, Z. Vuckovic, C. J. Draper-Joyce, Y.-L. Liang, A. Glukhova, A. Christopoulos, P. M. Sexton, Recent advances in the determination of G protein-coupled receptor structures. *Curr. Opin. Struct. Biol.* **51**, 28–34 (2018).
3. N. M. Delos Santos, L. A. Gardner, S. W. White, S. W. Bahouth, Characterization of the residues in helix 8 of the human β₁-adrenergic receptor that are involved in coupling the receptor to G proteins. *J. Biol. Chem.* **281**, 12896–12907 (2006).
4. S. Anavi-Goffer, D. Fleischer, D. P. Hurst, D. L. Lynch, J. Barnett-Norris, S. Shi, D. L. Lewis, S. Mukhopadhyay, A. C. Howlett, P. H. Reggio, M. E. Abood, Helix 8 Leu in the CB₁ cannabinoid receptor contributes to selective signal transduction mechanisms. *J. Biol. Chem.* **282**, 25100–25113 (2007).
5. J. Huynh, W. G. Thomas, M.-I. Aguilar, L. K. Pattenden, Role of helix 8 in G protein-coupled receptors based on structure-function studies on the type 1 angiotensin receptor. *Mol. Cell. Endocrinol.* **302**, 118–127 (2009).
6. J. Feierler, M. Wirth, B. Welte, S. Schüssler, M. Jochum, A. Faussner, Helix 8 plays a crucial role in bradykinin B₂ receptor trafficking and signaling. *J. Biol. Chem.* **286**, 43282–43293 (2011).
7. R. G. Kaye, J. W. Saldanha, Z.-L. Lu, E. C. Hulme, Helix 8 of the M₁ muscarinic acetylcholine receptor: Scanning mutagenesis delineates a G protein recognition site. *Mol. Pharmacol.* **79**, 701–709 (2011).
8. R. Sounier, C. Mas, J. Steyaert, T. Laeremans, A. Manglik, W. Huang, B. K. Kobilka, H. Déméné, S. Granier, Propagation of conformational changes during μ-opioid receptor activation. *Nature* **524**, 375–378 (2015).
9. J. J. Liu, R. Horst, V. Katritch, R. C. Stevens, K. Wüthrich, Biased signaling pathways in β₂-adrenergic receptor characterized by ¹⁹F-NMR. *Science* **335**, 1106–1110 (2012).
10. C. Altenbach, K. Cai, H. Gobind Khorana, W. L. Hubbell, Structural features and light-dependent changes in the sequence 306–322 extending from helix VII to the palmitoylation sites in rhodopsin: A site-directed spin-labeling study. *Biochemistry* **38**, 7931–7937 (1999).
11. C. Altenbach, A. K. Kusnetzow, O. P. Ernst, K. P. Hofmann, W. L. Hubbell, High-resolution distance mapping in rhodopsin reveals the pattern of helix movement due to activation. *Proc. Natl. Acad. Sci. U.S.A.* **105**, 7439–7444 (2008).
12. K. Kirchberg, T.-Y. Kim, M. Möller, D. Skegrov, G. Dasara Raju, J. Granzin, G. Büldt, R. Schlesinger, U. Alexiev, Conformational dynamics of helix 8 in the GPCR rhodopsin controls arrestin activation in the desensitization process. *Proc. Natl. Acad. Sci. U.S.A.* **108**, 18690–18695 (2011).
13. J. F. White, N. Noinaj, Y. Shibata, J. Love, B. Kloss, F. Xu, J. Gvozdenovic-Jeremic, P. Shah, J. Shiloach, C. G. Tate, R. Grisshammer, Structure of the agonist-bound neurotensin receptor. *Nature* **490**, 508–513 (2012).
14. P. Egloff, M. Hillenbrand, C. Klenk, A. Batyuk, P. Heine, S. Balada, K. M. Schlinkmann, D. J. Scott, M. Schütz, A. Plückthun, Structure of signaling-competent neurotensin receptor 1 obtained by directed evolution in *Escherichia coli*. *Proc. Natl. Acad. Sci. U.S.A.* **111**, E655–E662 (2014).
15. B. E. Krumm, J. F. White, P. Shah, R. Grisshammer, Structural prerequisites for G-protein activation by the neurotensin receptor. *Nat. Commun.* **6**, 7895 (2015).
16. B. E. Krumm, S. Lee, S. Bhattacharya, I. Botos, C. F. White, H. Du, N. Vaidehi, R. Grisshammer, Structure and dynamics of a constitutively active neurotensin receptor. *Sci. Rep.* **6**, 38564 (2016).
17. P. M. Dijkman, O. K. Castell, A. D. Goddard, J. C. Munoz-Garcia, C. de Graaf, M. I. Wallace, A. Watts, Dynamic tuneable G protein-coupled receptor monomer-dimer populations. *Nat. Commun.* **9**, 1710 (2018).
18. J. Oates, B. Faust, H. Attrill, P. Harding, M. Orwick, A. Watts, The role of cholesterol on the activity and stability of neurotensin receptor 1. *Biochim. Biophys. Acta* **1818**, 2228–2233 (2012).
19. A. K. Kusnetzow, C. Altenbach, W. L. Hubbell, Conformational states and dynamics of rhodopsin in micelles and bilayers. *Biochemistry* **45**, 5538–5550 (2006).
20. H.-T. Cheng, Megha, E. London, Preparation and properties of asymmetric vesicles that mimic cell membranes: Effect upon lipid raft formation and transmembrane helix orientation. *J. Biol. Chem.* **284**, 6079–6092 (2009).
21. J. H. Freed, Theory of slowly tumbling ESR spectra for nitroxides, in *Spin Labeling: Theory and Applications*, L. J. Berliner, Ed. (Academic Press, 1976), vol. I, pp. 53–132.
22. B. Carpenter, C. G. Tate, Active state structures of G protein-coupled receptors highlight the similarities and differences in the G protein and arrestin coupling interfaces. *Curr. Opin. Struct. Biol.* **45**, 124–132 (2017).
23. S. Lee, S. Bhattacharya, C. G. Tate, R. Grisshammer, N. Vaidehi, Structural dynamics and thermostabilization of neurotensin receptor 1. *J. Phys. Chem. B* **119**, 4917–4928 (2015).
24. R. Rahmeh, M. Damian, M. Cottet, H. Orcel, C. Mendre, T. Durroux, K. S. Sharma, G. Durand, B. Pucci, E. Trinquet, J. M. Zwier, X. Deupi, P. Bron, J.-L. Banères, B. Mouillac, S. Granier, Structural insights into biased G protein-coupled receptor signaling revealed by fluorescence spectroscopy. *Proc. Natl. Acad. Sci. U.S.A.* **109**, 6733–6738 (2012).
25. J. F. Fay, D. L. Farrrens, Structural dynamics and energetics underlying allosteric inactivation of the cannabinoid receptor CB₁. *Proc. Natl. Acad. Sci. U.S.A.* **112**, 8469–8474 (2015).
26. H. E. Kato, Y. Zhang, H. Hu, C.-M. Suomivuori, F. M. N. Kadji, J. Aoki, K. K. Kumar, R. Fonseca, D. Hilger, W. Huang, N. R. Latorraca, A. Inoue, R. O. Dror, B. K. Kobilka, G. Skiniotis, Conformational transitions of a neurotensin receptor 1–G_{i1} complex. *Nature* **572**, 80–85 (2019).
27. M. Najimi, P. Gailly, J. M. Maloteaux, E. Hermans, Distinct regions of C-terminus of the high affinity neurotensin receptor mediate the functional coupling with pertussis toxin sensitive and insensitive G-proteins. *FEBS Lett.* **512**, 329–333 (2002).

28. A. Kumar, A. Plückthun, In vivo assembly and large-scale purification of a GPCR-G α fusion with G $\beta\gamma$, and characterization of the active complex. *PLOS ONE* **14**, e0210131 (2019).
29. J. García-Nafria, C. G. Tate, Cryo-EM structures of GPCRs coupled to G s , G i and G o . *Mol. Cell. Endocrinol.* **488**, 1–13 (2019).
30. A. Manglik, T. H. Kim, M. Masureel, C. Altenbach, Z. Yang, D. Hilger, M. T. Lerch, T. S. Kobilka, F. S. Thian, W. L. Hubbell, R. S. Prosser, B. K. Kobilka, Structural insights into the dynamic process of β_2 -adrenergic receptor signaling. *Cell* **161**, 1101–1111 (2015).
31. G. Choi, J. Guo, A. Makriyannis, The conformation of the cytoplasmic helix 8 of the CB1 cannabinoid receptor using NMR and circular dichroism. *Biochim. Biophys. Acta* **1668**, 1–9 (2005).
32. M. Katragadda, M. W. Maciejewski, P. L. Yeagle, Structural studies of the putative helix 8 in the human β_2 adrenergic receptor: An NMR study. *Biochim. Biophys. Acta* **1663**, 74–81 (2004).
33. S. Inagaki, R. Ghirlando, J. F. White, J. Gvozdenovic-Jeremic, J. K. Northup, R. Grisshammer, Modulation of the interaction between neurotensin receptor NTS1 and Gq protein by lipid. *J. Mol. Biol.* **417**, 95–111 (2012).
34. O. Sensoy, H. Weinstein, A mechanistic role of helix 8 in GPCRs: Computational modeling of the dopamine D2 receptor interaction with the GIPC1-PDZ-domain. *Biochim. Biophys. Acta* **1848**, 976–983 (2015).
35. B. Chini, M. Parenti, G-protein-coupled receptors, cholesterol and palmitoylation: Facts about fats. *J. Mol. Endocrinol.* **42**, 371–379 (2009).
36. Y. Heakal, M. P. Woll, T. Fox, K. Seaton, R. Levenson, M. Kester, Neurotensin receptor-1 inducible palmitoylation is required for efficient receptor-mediated mitogenic-signaling within structured membrane microdomains. *Cancer Biol. Ther.* **12**, 427–435 (2011).
37. P. J. Stansfeld, J. E. Goose, M. Caffrey, E. P. Carpenter, J. L. Parker, S. Newstead, M. S. P. Sansom, MemProtMD: Automated insertion of membrane protein structures into explicit lipid membranes. *Structure* **23**, 1350–1361 (2015).
38. H. Koldø, D. Shorthouse, J. Hélie, M. S. P. Sansom, Lipid clustering correlates with membrane curvature as revealed by molecular simulations of complex lipid bilayers. *PLOS Comput. Biol.* **10**, e1003911 (2014).
39. T. A. Wassenaar, H. I. Ingólfsson, R. A. Böckmann, D. P. Tieleman, S. J. Marrink, Computational lipidomics with *insane*: A versatile tool for generating custom membranes for molecular simulations. *J. Chem. Theory Comput.* **11**, 2144–2155 (2015).
40. J. K. Kruschke, Bayesian estimation supersedes the t test. *J. Exp. Psychol. Gen.* **142**, 573–603 (2013).
41. V. Isberg, B. Vroling, R. van der Kant, K. Li, G. Vriend, D. Gloriam, GPCRDB: An information system for G protein-coupled receptors. *Nucleic Acids Res.* **42**, D422–D425 (2014).
42. G. E. Crooks, G. Hon, J.-M. Chandonia, S. E. Brenner, WebLogo: A sequence logo generator. *Genome Res.* **14**, 1188–1190 (2004).
43. R. K. Y. Cheng, E. Segala, N. Robertson, F. Deflorian, A. S. Doré, J. C. Errey, C. Fiez-Vandal, F. H. Marshall, R. M. Cooke, Structures of human A₁ and A_{2A} adenosine receptors with xanthines reveal determinants of selectivity. *Structure* **25**, 1275–1285.e4 (2017).
44. H. Zhang, H. Unal, R. Desnoyer, G. W. Han, N. Patel, V. Katritch, S. S. Karnik, V. Cherezov, R. C. Stevens, Structural basis for ligand recognition and functional selectivity at angiotensin receptor. *J. Biol. Chem.* **290**, 29127–29139 (2015).
45. R. Taniguchi, A. Inoue, M. Sayama, A. Uwamizu, K. Yamashita, K. Hirata, M. Yoshida, Y. Tanaka, H. E. Kato, Y. Nakada-Nakura, Y. Otani, T. Nishizawa, T. Doi, T. Ohwada, R. Ishitani, J. Aoki, O. Nureki, Structural insights into ligand recognition by the lysophosphatidic acid receptor LPA₆. *Nature* **548**, 356–360 (2017).
46. D. Zhang, Z.-G. Gao, K. Zhang, E. Kiselev, S. Crane, J. Wang, S. Paolletta, C. Yi, L. Ma, W. Zhang, G. W. Han, H. Liu, V. Cherezov, V. Katritch, H. Jiang, R. C. Stevens, K. A. Jacobson, Q. Zhao, B. Wu, Two disparate ligand-binding sites in the human P2Y₁ receptor. *Nature* **520**, 317–321 (2015).
47. K. Zhang, J. Zhang, Z.-G. Gao, D. Zhang, L. Zhu, G. W. Han, S. M. Moss, S. Paolletta, E. Kiselev, W. Lu, G. Fenalti, W. Zhang, C. E. Müller, H. Yang, H. Jiang, V. Cherezov, V. Katritch, K. A. Jacobson, R. C. Stevens, B. Wu, Q. Zhao, Structure of the human P2Y₁₂ receptor in complex with an antithrombotic drug. *Nature* **509**, 115–118 (2014).
48. C. Cao, Q. Tan, C. Xu, L. He, L. Yang, Y. Zhou, Y. Zhou, A. Qiao, M. Lu, C. Yi, G. W. Han, X. Wang, X. Li, H. Yang, Z. Rao, H. Jiang, Y. Zhao, J. Liu, R. C. Stevens, Q. Zhao, X. C. Zhang, B. Wu, Structural basis for signal recognition and transduction by platelet-activating-factor receptor. *Nat. Struct. Mol. Biol.* **25**, 488–495 (2018).
49. C. Zhang, Y. Srinivasan, D. H. Arlow, J. J. Fung, D. Palmer, Y. Zheng, H. F. Green, A. Pandey, R. O. Dror, D. E. Shaw, W. I. Weis, S. R. Coughlin, B. K. Kobilka, High-resolution crystal structure of human protease-activated receptor 1. *Nature* **492**, 387–392 (2012).
50. A. Luginina, A. Gusach, E. Marin, A. Mishin, R. Brouillette, P. Popov, A. Shiriaeva, É. Besserer-Offroy, J.-M. Longpré, E. Lyapina, A. Ishchenko, N. Patel, V. Polovinkin, N. Safranova, A. Bogorodskiy, E. Edelweiss, H. Hu, U. Weierstall, W. Liu, A. Batyuk, V. Gordeliy, G. W. Han, P. Sarret, V. Katritch, V. Borshchevskiy, V. Cherezov, Structure-based mechanism of cysteinyl leukotriene receptor inhibition by antiasthmatic drugs. *Sci. Adv.* **5**, eaax2518 (2019).
51. A. Gusach, A. Luginina, E. Marin, R. L. Brouillette, É. Besserer-Offroy, J.-M. Longpré, A. Ishchenko, P. Popov, N. Patel, T. Fujimoto, T. Maruyama, B. Stauch, M. Ergasheva, D. Romanovskaya, A. Stepko, K. Kovalev, M. Shevtsov, V. Gordeliy, G. W. Han, V. Katritch, V. Borshchevskiy, P. Sarret, A. Mishin, V. Cherezov, Structural basis of ligand selectivity and disease mutations in cysteinyl leukotriene receptors. *Nat. Commun.* **10**, 5573 (2019).
52. Y. Zhou, C. Cao, L. He, X. Wang, X. C. Zhang, Crystal structure of dopamine receptor D4 bound to the subtype selective ligand, L745870. *eLife* **8**, e48822 (2019).
53. A.-K. Apel, R. K. Y. Cheng, C. S. Tautermann, M. Brauchle, C.-Y. Huang, A. Pautsch, M. Hennig, H. Nar, G. Schnapp, Crystal structure of CC chemokine receptor 2A in complex with an orthosteric antagonist provides insights for the design of selective antagonists. *Structure* **27**, 427–438.e5 (2019).
54. T. Che, S. Majumdar, S. A. Zaidi, P. Ondachi, J. D. McCorry, S. Wang, P. D. Mosier, R. Uperty, E. Vardy, B. E. Krumm, G. W. Han, M.-Y. Lee, E. Pardon, J. Steyaert, X.-P. Huang, R. T. Strachan, A. R. Tribö, G. W. Pasternak, F. I. Carroll, R. C. Stevens, V. Cherezov, V. Katritch, D. Wacker, B. L. Roth, Structure of the nanobody-stabilized active state of the kappa opioid receptor. *Cell* **172**, 55–67.e15 (2018).
55. H. Zhang, G. W. Han, A. Batyuk, A. Ishchenko, K. L. White, N. Patel, A. Sadybekov, B. Zamlynny, M. T. Rudd, K. Hollenstein, A. Tolstikova, T. A. White, M. S. Hunter, U. Weierstall, W. Liu, K. Babaoglu, E. L. Moore, R. D. Katz, J. M. Shipman, M. Garcia-Calvo, S. Sharma, P. Sheth, S. M. Soisson, R. C. Stevens, V. Katritch, V. Cherezov, Structural basis for selectivity and diversity in angiotensin II receptors. *Nature* **544**, 327–332 (2017).
56. H. Asada, S. Horita, K. Hirata, M. Shiroishi, Y. Shiimura, H. Iwanari, T. Hamakubo, T. Shimamura, N. Nomura, O. Kusano-arai, T. Uemura, C. Suno, T. Kobayashi, S. Iwata, Crystal structure of the human angiotensin II type 2 receptor bound to an angiotensin II analog. *Nat. Struct. Mol. Biol.* **25**, 570–576 (2018).
57. T. Hori, T. Okuno, K. Hirata, K. Yamashita, Y. Kawano, M. Yamamoto, M. Hato, M. Nakamura, T. Shimizu, T. Yokomizo, M. Miyano, S. Yokoyama, Na⁺-mimicking ligands stabilize the inactive state of leukotriene B₄ receptor BLT1. *Nat. Chem. Biol.* **14**, 262–269 (2018).
58. B. Wu, E. Y. T. Chien, C. D. Mol, G. Fenalti, W. Liu, V. Katritch, R. Abagyan, A. Brooun, P. Wells, F. C. Bi, D. J. Hamel, P. Kuhn, T. M. Handel, V. Cherezov, R. C. Stevens, Structures of the CXCR4 chemokine GPCR with small-molecule and cyclic peptide antagonists. *Science* **330**, 1066–1071 (2010).
59. L. Qin, I. Kufareva, L. G. Holden, C. Wang, Y. Zheng, C. Zhao, G. Fenalti, H. Wu, G. W. Han, V. Cherezov, R. Abagyan, R. C. Stevens, T. M. Handel, Crystal structure of the chemokine receptor CXCR4 in complex with a viral chemokine. *Science* **347**, 1117–1122 (2015).
60. J. Lu, N. Byrne, J. Wang, G. Bricogne, F. K. Brown, H. R. Chobanian, S. L. Colletti, J. Di Salvo, B. Thomas-Fowlkes, Y. Guo, D. L. Hall, J. Hadix, N. B. Hastings, J. D. Hermes, T. Ho, A. D. Howard, H. Josien, M. Kornienko, K. J. Lumb, M. W. Miller, S. B. Patel, B. Pio, C. W. Plummer, B. S. Sherborne, P. Sheth, S. Souza, S. Tummala, C. Vonrhein, M. Webb, S. J. Allen, J. M. Johnston, A. B. Weinglass, S. Sharma, S. M. Soisson, Structural basis for the cooperative allosteric activation of the free fatty acid receptor GPR40. *Nat. Struct. Mol. Biol.* **24**, 570–577 (2017).
61. A. Srivastava, J. Yano, Y. Hirozane, G. Kefala, F. Gruswitz, G. Snell, W. Lane, A. Ivetac, K. Aertgeerts, J. Nguyen, A. Jennings, K. Okada, High-resolution structure of the human GPR40 receptor bound to allosteric agonist TAK-875. *Nature* **513**, 124–127 (2014).
62. J. D. Ho, B. Chau, L. Rodgers, F. Lu, K. L. Wilbur, K. A. Otto, Y. Chen, M. Song, J. P. Riley, H.-C. Yang, N. A. Reynolds, S. D. Kahl, A. Patel Lewis, C. Grospong, R. E. Madsen, K. Conners, J. P. Lineswala, T. Gheyi, M.-B. Decipulo Safor, M. R. Lee, J. Benach, K. A. Baker, C. Montrose-Rafizadeh, M. J. Genin, A. R. Miller, C. Hamdouchi, Structural basis for GPR40 allosteric agonism and incretin stimulation. *Nat. Commun.* **9**, 1645 (2018).
63. N. Srerama, S. Y. Venyaminov, R. W. Woody, Estimation of the number of α -helical and β -strand segments in proteins using circular dichroism spectroscopy. *Protein Sci.* **8**, 370–380 (1999).
64. L. Whitmore, B. A. Wallace, DICHROWEB, an online server for protein secondary structure analyses from circular dichroism spectroscopic data. *Nucleic Acids Res.* **32**, W668–W673 (2004).
65. M. A. Andrade, P. Chacón, J. J. Merelo, F. Morán, Evaluation of secondary structure of proteins from UV circular dichroism spectra using an unsupervised learning neural network. *Protein Eng.* **6**, 383–390 (1993).
66. S. W. Provencher, J. Glöckner, Estimation of globular protein secondary structure from circular dichroism. *Biochemistry* **20**, 33–37 (1981).
67. L. A. Compton, W. C. Johnson Jr., Analysis of protein circular dichroism spectra for secondary structure using a simple matrix multiplication. *Anal. Biochem.* **155**, 155–167 (1986).
68. N. Srerama, R. W. Woody, A self-consistent method for the analysis of protein secondary structure from circular dichroism. *Anal. Biochem.* **209**, 32–44 (1993).
69. A. Abdul-Gader, A. J. Miles, B. A. Wallace, A reference dataset for the analyses of membrane protein secondary structures and transmembrane residues using circular dichroism spectroscopy. *Bioinformatics* **27**, 1630–1636 (2011).
70. J. G. Lees, A. J. Miles, F. Wien, B. A. Wallace, A reference database for circular dichroism spectroscopy covering fold and secondary structure space. *Bioinformatics* **22**, 1955–1962 (2006).

71. N. Sreerama, S. Y. Venyaminov, R. W. Woody, Estimation of protein secondary structure from circular dichroism spectra: Inclusion of denatured proteins with native proteins in the analysis. *Anal. Biochem.* **287**, 243–251 (2000).
72. D. Mao, E. Wachter, B. A. Wallace, Folding of the mitochondrial proton adenosine triphosphatase proteolipid channel in phospholipid vesicles. *Biochemistry* **21**, 4960–4968 (1982).

Acknowledgments: We thank the Centre of Advanced ESR (CAESR, University of Oxford) for access to EPR equipment and technical support, D. Staunton (University of Oxford) for technical support, P. Judge (University of Oxford) and S. van Weezel (Radboud University) for helpful discussion, and X. Zhao (East China Normal University) for giving us access to the Shanghai Supercomputer Center. We further acknowledge the high-performance computing resources provided by the Structural Bioinformatics and Computational Biochemistry unit (University of Oxford), the e-Infrastructure South Consortium Emerald cluster, and the Advanced Research Computing ARCUS cluster (University of Oxford). This project made use of time on ARCHER and JADE granted via the UK High-End Computing Consortium for Biomolecular Simulation, HECBioSim (www.hecbiosim.ac.uk/), supported by EPSRC (grant no. EP/R029407/1). **Funding:** This work was financially supported by the Medical Research Council (grant no. G0900076 to A.W., MR/S009213/1 to P.J.S., and studentship to S.R.L.), the Biotechnology and Biological Sciences Research Council (grant nos. BB/P01948X/1, BB/R002517/1, and BB/S003339/1 to P.J.S.), Wellcome (208361/Z/17/Z to P.J.S.), and UCB Celltech

(to A.W.). P.S.K. and A.J.C.-F. thank FAPESP (grant nos. 2010/17662-8, 2011/21767-2, and 2012/20358-4) and CNPq. **Author contributions:** P.M.D. established the protocol for the site-directed spin labeling of NTS1 and associated EPR experiments, which were conducted by P.M.D., S.R.L., and P.S.K. P.M.D. analyzed the EPR data with input from S.R.L. P.M.D. conducted the CD experiments. J.C.M.-G. prepared the models for MD simulations. J.C.M.-G. and P.J.S. performed MD simulations. J.C.M.-G. and P.M.D. analyzed the MD results. R.I.d.R. conducted the NTS1 signaling studies and analysis. D.Y. designed and conducted EPR experiments with spin-labeled lipids. P.M.D., S.R.L., J.C.M.-G., R.I.d.R., and D.Y. wrote the manuscript with input from the other authors. A.J.C.-F. and A.W. supervised the project and secured the funding.

Competing interests: The authors declare that they have no competing interests. **Data and materials availability:** All data needed to evaluate the conclusions in the paper are present in the paper and/or the Supplementary Materials. Additional data related to this paper may be requested from the authors.

Submitted 23 October 2018

Accepted 2 July 2020

Published 14 August 2020

10.1126/sciadv.aav8207

Citation: P. M. Dijkman, J. C. Muñoz-García, S. R. Lavington, P. S. Kumagai, R. I. dos Reis, D. Yin, P. J. Stansfeld, A. J. Costa-Filho, A. Watts, Conformational dynamics of a G protein-coupled receptor helix 8 in lipid membranes. *Sci. Adv.* **6**, eaav8207 (2020).

Conformational dynamics of a G protein–coupled receptor helix 8 in lipid membranes

Patricia M. Dijkman, Juan C. Muñoz-García, Steven R. Lavington, Patricia Suemy Kumagai, Rosana I. dos Reis, Daniel Yin, Phillip J. Stansfeld, Antonio José Costa-Filho and Anthony Watts

Sci Adv **6** (33), eaav8207.
DOI: 10.1126/sciadv.aav8207

ARTICLE TOOLS

<http://advances.sciencemag.org/content/6/33/eaav8207>

SUPPLEMENTARY MATERIALS

<http://advances.sciencemag.org/content/suppl/2020/08/11/6.33.eaav8207.DC1>

REFERENCES

This article cites 71 articles, 17 of which you can access for free
<http://advances.sciencemag.org/content/6/33/eaav8207#BIBL>

PERMISSIONS

<http://www.sciencemag.org/help/reprints-and-permissions>

Use of this article is subject to the [Terms of Service](#)

Science Advances (ISSN 2375-2548) is published by the American Association for the Advancement of Science, 1200 New York Avenue NW, Washington, DC 20005. The title *Science Advances* is a registered trademark of AAAS.

Copyright © 2020 The Authors, some rights reserved; exclusive licensee American Association for the Advancement of Science. No claim to original U.S. Government Works. Distributed under a Creative Commons Attribution NonCommercial License 4.0 (CC BY-NC).